ROYAL SOCIETY OF CHEMISTRY

PAPER

Check for updates

Micromagnetic structure of oxidized magnetite nanoparticles: sharp structural *versus* diffuse magnetic interface

Elizabeth M. Jefremovas, [ID] *[a,b] Michael P. Adams, [ID] [a] Lucía Gandarias, [ID] [c] Lourdes Marcano, [ID] [d,e] Javier Alonso, [ID] [f] Andreas Michels [ID] [a] and Jonathan Leliaert [ID] [g]

The oxidation of magnetite to maghemite is a naturally occurring process that leads to the degradation of the magnetic properties of magnetite nanoparticles. Despite being systematically observed with traditional macroscopic magnetization measurement techniques, a detailed understanding of this process at the microscale is still missing. In this study, we track the evolution of the magnetic structure of magnetite nanoparticles during their oxidation to maghemite through numerical micromagnetic simulations. To capture realistic interparticle effects, we incorporate dipolar interactions by modeling the nanoparticles arranged in chains. Our computational results are benchmarked against experimental data from magneto-tactic bacteria, studied over a time scale of years. To resolve the magnetization at the interface between both oxide phases, we propose spin-polarized small-angle neutron scattering (SANS), an experimental technique capable of probing magnetization textures at nanometer length scales. By analyzing the pair-distance distribution function extracted from numerically-computed SANS cross sections, we identify distinct signatures of magnetic disorder. Specifically, our findings suggest that the magnetization from the non-oxidized core region varies smoothly across the (structurally sharp) interface into the oxidized shell. The existence of such a diffuse magnetic interface may account for the superior magnetic properties of partially oxidized magnetite nanoparticles compared to fully converted maghemite samples.

1. Introduction

Magnetic nanoparticles (MNPs) are one of the leading agents of the new medicine era.[1–5] With highly tunable properties and particle sizes of the order of biological entities (*e.g.*, proteins, nucleid acids, viruses), their sizable magnetic moment allows, for example, the external activation using alternating magnetic fields, in this way enabling the remote generation of localized heat. In a therapeutic approach known as magnetic hyperthermia (MHT) this heat is harnessed to selectively destroy or debilitate cancerous cells (see, *e.g.*, ref. 6–11 and references therein).

During the last years extensive efforts have been devoted to the engineering of magnetite MNPs with maximized heat release.[12–15] The knowledge gathered so far points to the arrangement of magnetite MNPs in a chain configuration, which can be induced remotely in cubic morphologies,[16] as one of the top-notch arrangement in terms of bio-compatibility and maximized heat release during MHT treatments.[17–21] However, there is a crucial aspect preventing the direct translation of these improved MNP designs into clinical results, which is the inevitable oxidation of iron oxide MNPs over the time scale between their synthesis and the clinical treatment. This naturally-occurring process occurring in ambient atmosphere on time scales of weeks or months,[22–25] prevents single domain particles to reach their maximum magnetic moment per volume,[26] falling their magnetization below the one of the bulk,[27] with the ensuing deterioration of the heating efficiency.[24,28] Connecting the kinetics of oxidation to the MNP macroscopic magnetization is key towards biomedical applications, as this process is sped-up for MNPs that are

[a]Department of Physics and Materials Science, University of Luxembourg, 162A Avenue de la Faiencerie, L-1511 Luxembourg, Grand Duchy of Luxembourg. E-mail: elizabeth.jefremovas@uni.lu
[b]Institute for Advanced Studies, University of Luxembourg, Campus Belval, L-4365 Esch-sur-Alzette, Luxembourg
[c]Aix-Marseille Université, CEA, CNRS, BIAM, 13115 Saint Paul lez Durance, France
[d]Center for Cooperative Research in Biomaterials (CIC biomaGUNE), Basque Research and Technology Alliance, Donostia-San Sebastián 20014, Spain
[e]Physics Department, University of Oviedo, C/Calvo Sotelo, s/n., 33007 Oviedo, Spain
[f]Department CITIMAC, Faculty of Sciences, University of Cantabria, 39005 Santander, Spain
[g]DyNaMat, Department of Solid State Sciences, Ghent University, 9000 Ghent, Belgium

located within the tumoral area owing to their acid conditions, reducing the oxidation time scale to days.[29–31] This is a major concern for MHT, since the lost of magnetization requires the on-the-flow adjustment of the treatment, with a possible re-injection of MNPs after only 6 days.[31]

In our work, we micromagnetically investigate progressively oxidized magnetite cubic MNP chains to gain insight in the concurrent magnetic degradation of the properties. Starting from a purely magnetite composition, with a defined uniaxial anisotropy direction K_u, we model the effect of oxidation by including a maghemite shell of variable thickness δ, which comprises random anisotropy directions. To ensure relevance to experimental systems, we follow the oxidation process of bacterial magnetosomes, *i.e.*, pure magnetite MNPs biominera-lized by magnetotactic bacteria (MTB),[32–37] keeping them intracellular over a time scale of years, using the measured values of the magnetic materials parameters as input for the simulations. Based on the numerical results for the spin structure, we compute the small-angle neutron scattering (SANS) cross section and the related pair-distance distribution function. This allows us to identify the characteristic signatures of magnetic disorder and to resolve the magnetic correlations at the core@shell interface.[38–42]

The article is organized as follows: in section 2, we introduce the materials and methods used in this study. Section 3 discusses the results, with section 3.1 presenting the experimental results that are used as input for the material parameters in the micromagnetic simulations. In section 3.2, we discuss the results of the numerical micromagnetic calculations, which are used to model the progressive formation of the maghemite shell. This is done by calculating the coercivity and by comparing the results for different layer thicknesses δ. In section 3.3, we show the neutron scattering results for the pair-distance distribution function $p(r)$. We consider that $p(r)$ is an important quantity where the most pronounced effect of the interface-thickness variation becomes visible and that can also be easily detected experimentally. Finally, section 4 summarizes the main findings of this work. The SI[43] provides further details on the structural and magnetic characterization of the magnetite MNPs and the main expressions for the SANS observables.

2. Materials and methods

Magnetotactic bacteria *Magnetospirillum gryphiswaldense* (MSR-1) strain MSR-1 (DMSZ 6631) and *Magnetospirillum magneticum* (AMB-1) strain AMB-1 have been cultured microaerobi-cally at 28 °C in flask standard medium, as described by Heyen and Schüler,[44] and supplemented by 100 μM iron(III)-citrate to support magnetosome formation. Briefly, the culture was carried out in 1 L bottles at 28 °C under microaerobic conditions (bottles loosely closed and without shaking for MSR-1; and bottles filled to the top and with the caps completely closed for AMB-1). Cells were collected after 96 h when well-formed magnetosomes were present.[36] The cells were har-

vested by centrifugation (8000g, 15 minutes, 4 °C) and the pellets were resuspended in PBS and fixed with 2% glutaralde-hide overnight. Then, the bacteria were washed 3 times with PBS and 2 times with filtered MilliQ water. Lastly, the bacterial pellets were freeze-dried, resulting in a powder sample. The samples were kept at room temperature under vacuum (base pressure $p \lesssim 8.8 \times 10^{-2}$ mbar) for the whole duration of the study.

DC magnetization measurements were performed using a Quantum Design QD-MPMS SQUID magnetometer in the temperature range between 5–300 K. The samples consist of magnotosome chains kept within the bacteria body, each of the bacteria randomly oriented with respect to each other. $M(T)$ curves were measured from 10 to 300 K, following a zero-field-cooling/field-cooling protocol (ZFC–FC): the samples were cooled in the absence of an applied field from 300 K to 5 K. At 5 K, a fixed magnetic field of 5 mT was applied and the magnetization was measured upon warming to 300 K (ZFC). With the field still on, the sample was cooled to 5 K and the magnetization was measured upon warming to 300 K (FC). $M(H)$ loops were measured at 300 K and 5 K for applied fields up to 2 T.

Micromagnetic simulations were performed using the software package MuMax3 (version 3.11).[45] The isotropic exchange interaction, an uniaxial magnetic anisotropy, the Zeeman energy as well as the magnetodipolar interaction have been taken into account. The following materials parameters were used: for the Fe_3O_4 phase, the saturation magnetization has been fixed to $M_s = 0.486$ MA m^{-1}, the exchange-stiffness constant to $A = 13$ pJ m^{-1}, and the uniaxial anisotropy constant was taken as H_c kJ m^{-3}, based on both experimental and literature data.[46–48] Note that, to capture the consequences of the oxidation, simulations have been performed at $T = 0$ K $\ll T_V$, where the anisotropy is dominated by the uniaxial K_u term with no influence of the cubic term K_c with $\langle 111 \rangle$ easy axes. For the maghemite phase, a reduced M_s of 0.412 MA m^{-1} has been assumed keeping the uniaxial anisotropy at its bulk value. The anisotropy direction of the magnetite phase has been fixed to follow the chain axis, which is oriented at angles between 12–20° relative to the crystallographic $\langle 111 \rangle$ direction.[49] In the present simulations, this angle has been fixed to 15°. To simulate the magnetically disordered environment of the maghemite phase, the surface region was subdivided into grains using a Voronoi tessellation.[50] This choice reflects experimental observations, which show that "fresh" magnetosomes retain a single-crystalline structure resembling the one of pure magnetite,[20,34,51] while the oxidation leads to the formation of a maghemite phase.[52] This results in a magnetite@maghemite core@shell nanoparticle with decreased crystallinity due to the formation of a surface layer with a similar structure of feroxyhite, introducing planar defects.[53] Modeling the oxidized shell as polycrystalline therefore provides a realistic approximation of the structural changes associated with the oxidation process. In our simulations, the shell then consists of a collection of grains, with size D, where the uniaxial anisotropy points into random directions. The exchange coupling at the intergrain boundaries has been reduced by a factor

$0 < k \leq 1$ to model the effect of magnetic disorder: A value of $0.75 \times A$ ($k = 0.75$) reproduces the experimental results well. The grain size D has been slightly varied to follow the shell thickness δ. The total nanoparticle dimensions (core plus shell thickness δ) are fixed at 48 nm along both short axes and 64 nm along the long axis. We employed a grain size of $D = 2$ nm for $\delta = 2$ nm, $D = 4$ nm for 4 nm and 8 nm shells, and $D = 5$ nm for $\delta = 5$ nm and 10 nm. The sample volume was discretized into cells with a typical size of 2 nm. This cell value is well below the exchange length $l_{ex} = \sqrt{2A/(\mu_0 M_s^2)} \cong 9.4$ nm, ensuring that nanometer-scale spatial variations of the magnetization can be resolved. The energy minimum was obtained by using the steepest descent method,[54] encoded in the "minimize" function of MuMax3. To reproduce the random orientations of the MNPs in the experiments, the external magnetic field $\vec{H}$ has been rotated from 0 to 90°, and we have repeated the simulations for 10 different random seeds to obtain statistically significant results.

The calculation of the polarized small-angle neutron scattering (SANS) observables follows the procedure detailed in ref. 39 and 55–58. Simulations were performed on a single, oriented cuboidal particle. Briefly, the resulting discrete real-space magnetization vector of the MNP, $\mathbf{M}_i(\mathbf{r}_i)$, where the subscript "$i$" refers to the ith cell, is Fourier transformed to obtain the magnetic SANS cross section for the particular scattering geometry, where the applied magnetic field is perpendicular to the incoming neutron beam. The magnetic scattering cross section on the two-dimensional detector is then averaged to obtain the one-dimensional SANS intensity profile $I_{sf}(q)$ from which the pair-distance distribution function $p(r)$ is numerically computed via Fourier transformation. In this paper, we have computed $p(r)$ results for the purely magnetic spin–flip SANS cross section, which can be obtained from uniaxial neutron polarization analysis experiments (e.g., ref. 59–63) and does not contain the nonmagnetic (structural) scattering contribution. See the SI[43] for further details.

3. Results and discussion

3.1. Magnetic properties of oxidized bacterial magnetosomes

We have followed the oxidation process of bacterial magnetosomes kept intracellular at a time scale of years, measuring the degradation of their magnetic properties. These values, together with the morphology of the bacteria at $t = 0$ (shown in the SI Fig. 1 and 2) are used as input material parameters to our simulations, connecting our calculations with experimental values.

In order to detect the variations of the magnetic properties with time, we have studied the same batch of MSR-1 and AMB-1 bacteria, starting at $t = 0$ (fresh bacteria) along a long period of time (3 and 6 years for MSR-1 and 1.5 and 4 years for AMB-1). Unlike the reported studies with uncapped inorganically-synthesized magnetite nanoparticles,[23,24] the proteolipidic membrane of the magnetosomes, in addition to the bacterial body, acts as a strong barrier against oxidation, in this

way slowing down the oxidation process from a few months to years.

Fig. 1 features the magnetization data of MSR-1 and AMB-1 bacteria. Both $M(T)$ ZFC–FC curves exhibit a pronounced irreversibility throughout the entire temperature range, with a blocking temperature being above 300 K, consistent with the large size of the magnetosomes. Similarly, the ZFC curve of the two studied strains presents a sudden drop in the magnetization at T_V, a typical signature of the Verwey transition, which provides strong evidence for the presence of magnetite in the bacteria.[64,65] At $t = 0$, the T_V, extracted from the derivative of dM_{ZFC}/dT as in ref. 46 and 66, is found at 104 ± 2 K (106 ± 2 K for AMB-1), a value that is lower than the bulk value of magnetite ($T_V = 120$ K (ref. 64)), yet typically reported for magnetotactic bacteria.[36,46,48,66,67] The decrease with respect to the bulk value is usually ascribed to microstrain disorder, yielding slight distortions from the perfect bulk magnetite crystalline structure, which is supported by the nonzero microstrain value shown in our XRD analysis (see the SI[43]). After 1.5 years, this transition decreases by 7 K in AMB-1, remaining at $T_V = 98$ K after 4 years, thus, yielding a total reduction of ≈ 7.5 % after 4 years. This reduction is of the same order of magnitude as the one experienced by *M. griphyswaldense* after 3 years. In this case, the T_V decreases to $T_V = 95 \pm 2$ K, *i.e.*, $\approx 8.6\%$. The reduction of T_V is an indication of an oxidation process of magnetite to maghemite, since the latter does not undergo the Verwey transition on behalf of its lack of Fe^{2+} ions.[68–70] Further increase of time results in a further reduction of T_V, as expected from the reduced energy scale of the transition in the presence of the increased disorder due to the oxide shell. In this sense, MSR-1 reduces T_V to 88 K after 6 years, corresponding to an $\approx 15\%$ reduction of the initial value. It is interesting to note that the decrease in T_V obtained in both
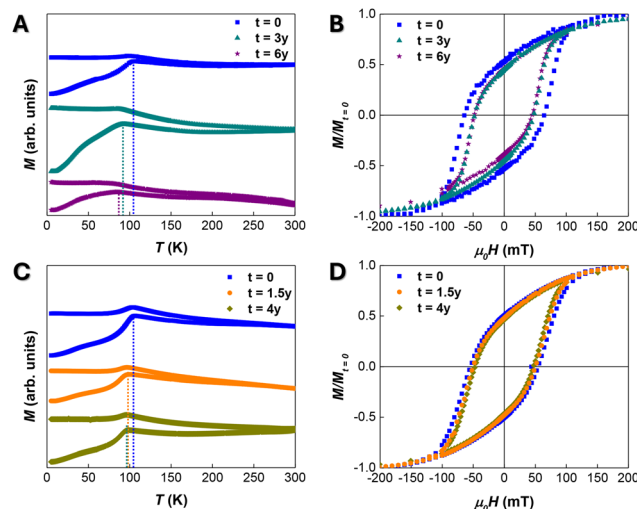

Fig. 1 (A) and (C) Zero-field-cooling/field-cooling (ZFC−FC) $M(T)$ curves for MSR-1 and AMB-1, respectively, measured at 0, 1.5, 3, 4, and 6 years. The position of the Verwey transition is marked by dotted vertical lines. (B) and (D) Hysteresis loops $M(H)$ measured at $T = 5$ K normalized by the value of $M(t = 0)$ for each bacterial strain.

samples is appreciably smaller than the one typically observed for synthetic magnetite MNPs; for example, Kim *et al.*[23] reported a ≈25% decrease of T_V in 44 nm magnetite MNPs after 3 years. This implies that, by preserving the magnetosomes inside the bacterial body, we successfully manage to slow down the oxidation process that naturally happens in magnetite.

The difference in the shape of the Verwey transition observed in the ZFC–FC curves of both bacterial strains also provides insights into the bacterial chain configuration. Unlike bulk magnetite, where the Verwey transition is sharp and abrupt, in magnetotactic bacteria, the magnetite MNPs are synthesized by living entities through a complex biomineralization process, which comprises a compendium of cellular processes involving a large set of specialized genes.[71–76] As a result, inhomogeneities in the magnetosome shape and size occur, yielding a broader transition in the ZFC–FC curves compared to bulk magnetite.[64] Note particularly the case of MSR-1 in Fig. 1(A). As introduced in the previous section, the biomineralization process of MSR-1 and AMB-1 are different, as the former tends to grow magnetosomes arranged in one single long chain, whereas the latter tends to nucleate magnetosomes at different positions, forming smaller chains.[35,36,71,77–79] This results in a broader size distribution of the magnetosomes for MSR-1, and thus, in a broader Verwey transition compared to the one of AMB-1.

To capture the consequences of the oxidation, we have analyzed the measurements performed at $T = 10$ K $\ll T_V$, where the anisotropy is dominated by the uniaxial K_u term. Above T_V, the magnetocrystalline anisotropy is dominated by the cubic term K_c with $\langle 111 \rangle$ easy axes, which is less sensitive to structural distortions or surface oxidation, especially when magnetite remains the dominant phase. We refer the reader to the SI,[43] where the comparison between the hysteresis loops at $T = 300$ K for MSR-1 measured at $t = 0$ and $t = 6$ years is provided.

Fig. 1(B) and (D) include the $M(H)$ hysteresis loops measured at $T = 10$ K, for MSR-1 and AMB-1, respectively. At such a temperature, the anisotropy is dominated by the uniaxial term K_u. A reduction of the coercive field, H_c, can be detected, serving as an indication of the presence of a disordered surface at the magnetosomes.[80,81] In this way, for MSR-1, H_c reduces from 64 mT to 49 mT after 3 years, *i.e.*, almost by 25%. Measurements carried out after 6 years indicate no significant further oxidation, and the H_c value stays almost constant (48 mT). For AMB-1, H_c reduces from 54 mT to 50 mT after 1.5 years, and further to 47 mT after 4 years, *i.e.*, a reduction of almost 15% of the initial value. The presence of smaller magnetosomes in the chains of MSR-1, more sensitive to oxidation on behalf of their larger surface-to-volume ratio, could account for this difference.

3.2. Micromagnetic simulations of magnetite@maghemite nanoparticles

Our magnetic measurements provide indirect evidence for the oxidation of the magnetosomes. This finding is based on: (i) a less abrupt and temperature-shifted Verwey transition and (ii)

a decreased coercivity at $T = 10$ K. To model and quantify the oxidation process by determining the amount of magnetite that transforms into maghemite, we have numerically simulated the hysteresis loops of individual magnetosomes and the chain arrangements. Our simulations approximate the magnetosomes as cuboids of dimensions $48 \times 48 \times 64$ nm^3. This geometry is also similar to the elongated magnetosomes of *M. blakemorei* strain,[82–84] and is representative for the magnetosomes studied in this work (see the SI[43] for TEM images). To account for the oxidation, we have simulated a core@shell structure, consisting of a large magnetite core with a defined uniaxial anisotropy direction that is surrounded by a polycrystalline surface layer of maghemite. We have included a sketch of our simulated cuboid chains in Fig. 2(A), which also reproduces the slight rotation of the magnetosomes (15°)[49] to make our model as close to reality as possible.

Fig. 2(B) features the hysteresis loops for $N = 1$, 3, and 9 cuboids arranged in chains for a pure magnetite phase (*i.e.*, no oxidation). We have performed our simulations at $T = 0$ K to remove the thermal noise and to closely mimic the $T = 5$ K experimental conditions. First, we observe a significant increase of the coercivity (by about 20%) when $N > 1$. This difference is triggered by the dipolar interaction between the cuboids. Comparing the $N = 3$ and $N = 9$ data, no significant differences are found ($\mu_0 H_c = 68$ mT and 69 mT, respectively). This indicates that an assembly of $N = 3$ cuboids with a defined shape anisotropy is already sufficient to benefit from dipolar interactions, with no further improvement by assembling more cuboids into the chain. Based on these results, we simplify the magnetosome chains by studying $N = 3$ cuboids arrangements, with the intrinsic advantage of reducing computational costs.

Fig. 2(C) includes the results of the hysteresis loops performed for the $N = 3$ chain for different Fe_2O_3 δ values. As it can be seen, H_c is progressively reduced upon increasing the oxidation layer. Given that the anisotropy direction of the oxidized layer is random in every grain, together with the lower saturation magnetization of maghemite, a softer magnetic behavior of the MNP ensemble is expected. We have determined the influence of the intergrain coupling by testing two values for the exchange weakening, $k = 0.25$ and 0.75, corresponding to low and high intergrain coupling scenarios, respectively. Although these values affect the absolute value of the coercivity, resulting in a lower coercivity for strongly-coupled grains, the trend followed by the decrease of the coercive field with increasing δ is similar in both cases (see Fig. 2(D)), indicating the crucial role of the deviations from the uniaxial anisotropy direction $\langle 111 \rangle$ in the coercivity reduction.

Fig. 2(D) summarizes our micromagnetic results. We present the coercive fields as a function of δ for $N = 1$ and 3 ($k = 0.25$ and 0.75), together with our experimental data. To facilitate the interpretation, we have normalized the H_c values to the coercivity at $\delta = 0$, corresponding to $t = 0$. The error bars, below 5%, reflect the average over 10 different random seeds per simulated angle. The decrease in coercivity as a function of δ is linear for both $N = 1$ and 3 configurations, in agreement
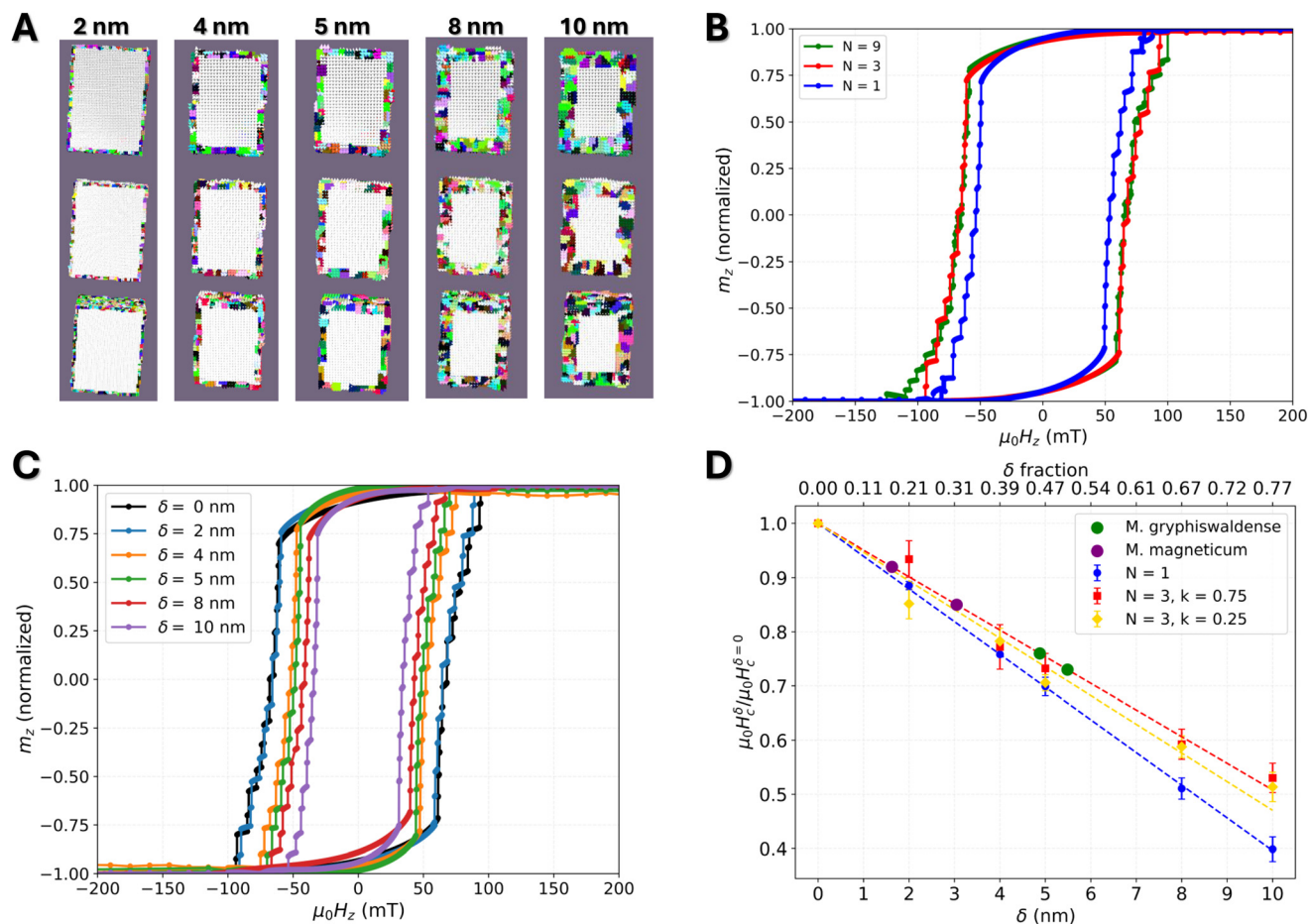
Fig. 2 (A) Microstructures of the simulated cuboid chains for different Fe_2O_3 shell thicknesses δ. The size of an individual particle is 48 × 48 × 64 nm, and panel (A) shows chains of $N = 3$ dipolarly-coupled particles. The color scheme represents the uniaxial anisotropy direction for all the magnetic cells. The ones within the magnetite core (white color) follow the $\langle 111 \rangle$ direction rotated by 15° with respect to the z axis to mimic the chain configuration.[49] For the maghemite shell, the direction of K_u is random in each grain, represented by the different colors. (B) Hysteresis loops for $N = 1$, 3, and 9 chains. The coercivity H_c increases from $N = 1$ to $N > 1$ with no significant differences between $N = 3$ and $N = 9$. (C) Simulated hysteresis loops for a chain of $N = 3$ cuboids for different δ. The coercive field H_c decreases as δ increases. (D) H_c versus layer thickness δ: values are calculated for $N = 1$ (blue), $N = 3$ with an intergrain exchange-coupling reduction of $k = 0.25$ (yellow), and $k = 0.75$ (red) cuboid chains. For clarity, the H_c values have been normalized to the value at $\delta = 0$ nm. H_c decreases linearly with δ. We have included the experimental data for *Magnetospirillum gryphiswaldense* and *Magnetospirillum magneticum* to estimate the δ agreeing with the observed H_c reduction.

with the expected behavior of single-domain MNPs within the first-order approximation of the Stoner-Wohlfarth model.[49,85,86] The linear fits are forced to intercept the point (0,1), as the $t = 0$ are assumed to be not oxidized. The absolute value of the slope is smaller for $N = 3$ compared to $N = 1$ (by a factor of ~0.88), which can be attributed to the enhanced net anisotropy term, that encloses both the intrinsic uniaxial anisotropy K_u and the dipolar interactions between the magnetosomes. This results reveals that, when oxidized MNPs are arranged in a chain, their average magnetization is similar to the one that individual less-oxidized MNPs. Therefore, preserving dipolar interactions among the MNPs would slow down the degradation of their magnetic properties over extended timescales compared to the isolated case. The data corresponding to $k = 0.25$ show a slightly faster decrease (factor ≈1.07) compared to the $k = 0.75$ case. The reduced inter-grain exchange coupling

enhances the pinning potentials, rendering the nanoparticle surface more susceptible to magnetic disorder.

Moreover, the intersection of our experimental data with the simulation results corresponding to $N = 3$ and $k = 0.75$ (dotted line in Fig. 2(D) allows to indirectly estimate the thickness of the oxidized layer in our samples). For MSR-1, we find oxidation percentages of approximately 45% and 50% after 3 and 6 years, respectively. In the case of AMB-1, the estimated oxidation levels are around 17% and 30% after 1.5 and 4 years, respectively. These values are unprecedented in comparison to existing literature, where oxidation rates exceeding 25% are typically reported after only days or months.[22–24] Even if the preservation protocol in our case differs from those of previous studies, often involving direct oxygen exposure or accelerated oxidation conditions, it is important to note that in our measurements the bacteria are exposed to air for several days,

which has been reported to be sufficient to initiate oxidation.[23,31] Particularly, in the study carried out by M. Widdrat *et al.*,[52] oxidation values close to 30% for magnetite samples preserved in contact with air or in air + Ar atmosphere are reported after 546 days (1.5 years). Such an oxidation rate is almost double the one of AMB-1 for the same timescale. The observed diminished oxidation in magnetosome chains kept intracellular over years highlights the exceptional long-term stability of magnetite nanoparticles when preserved forming chains inside bacteria.

We detect a significant slower degradation of AMB-1 compared to MSR-1, which we ascribe to the homogeneous size distribution of the former. In the SI,[43] we have analyzed the size distribution of both bacteria strains, finding a bimodal size distribution for MSR-1, centered at ≈15 and 43 nm. Whereas the larger MNPs have a reduced surface-to-volume ratio, reducing the impact of the oxidized shell, the smaller ones are more sensitive. As the macroscopic coercivity reflects an average of the individual contributions, oxidation effects are more present for the case of MSR-1 compared to AMB-1.

3.3. Fingerprints of shell disorder in polarized SANS

The present study shows that the degradation of the magnetic properties of magnetite nanoparticles is compatible with the oxidation of the magnetite phase. This is accomplished by (i) indirect experimental evidence, from the reduction of the Verwey transition and coercivity measured over the years, and by (ii) micromagnetic simulations, which successfully reproduce this coercivity decrease when a magnetite@maghemite core@shell microstructure is modeled. While the combination of these approaches provides an estimate for the maghemite shell thickness δ, only the direct experimental measurement of δ can validate such a hypothesis. Mössbauer spectroscopy is the experimental probe traditionally employed.[24,87–89] However, this technique, although already applied in tissue environments to probe their iron-content,[90] may not provide enough resolution to quantify the percentage of maghemite and magnetite for the case of MNPs kept intra-cellular, as the effective areal density of ^{57}Fe probed per volume is reduced (the iron mass fraction is small relative to the total cellular/organic matrix). This limits the counting statistics. Moreover, size polydispersity, cation disorder and partial oxidation can produce a line broadening and overlap, making it challenging to quantitatively deconvolve magnetite from maghemite fractions, and by extension, the quantification of a thin maghemite shell thickness δ.

To detect and quantify thin oxide layers in MNPs embedded in realistic environments we propose here the use of polarized small-angle neutron scattering (SANS). This technique provides volume-averaged information with a spatial resolution that covers the relevant mesoscopic length scale (a few up to a few hundreds of nanometers).[38–40,42,42,91] Many examples in the literature demonstrate the success of magnetic SANS to resolve and quantify the magnetization distribution within iron oxide MNPs (*e.g.*, ref. 38 and 92–94). Furthermore, SANS has already been employed in magnetotactic bacteria to resolve their magnetic chain morphology[49] and the rotation mechanism under applied fields,[95] validating this technique for the probe of MNPs embedded in cell environments.

Based on the real-space micromagnetic simulation results, we calculate the SANS observables for a single magnetite@maghemite cuboidal MNP for different values δ of the maghemite surface-layer thickness. More specifically, we model the signatures of oxidation in the real-space pair-distance distribution function $p(r)$ of the spin–flip SANS cross section. This function describes the distribution of real-space distances between volume elements inside the particle, weighted by the excess scattering length density function.[96] The spin–flip SANS cross section, from which we extract the $p(r)$ by Fourier transformation, can be measured in a uniaxial polarization analysis experiment (*e.g.*, ref. 59–63) and does not contain the unwanted structural (nuclear coherent) scattering contribution that could potentially mask the fingerprints of magnetically disordered interfaces.[39] Details regarding the micromagnetic SANS simulation procedure can be found in ref. 39 and 55–58.

Fig. 3(A) depicts a sketch of the scattering geometry. In our calculations, we have considered only a single oriented magnetosome, as the surface oxidation effects are more pronounced at the level of individual particles than in the full magnetosome chain. All simulations are initialized from the saturated magnetic configuration. The easy-axis anisotropy direction $\vec{K}_u$ is parallel (and antiparallel) to the $\vec{e}_y$ direction of a Cartesian laboratory coordinate system and perpendicular to the incoming neutron beam, which is parallel to $\vec{e}_x$. The externally applied magnetic field is along $\vec{e}_z$ ($\vec{H} \parallel \vec{e}_z$).

Fig. 3(B) features the computed $p(r)$ at remanence for the different δ values used in this work. We have included the results for a uniformly magnetized cuboid along its long axis as a reference for the ideal non-oxidized case (black dashed line). It is emphasized that the overall geometrical dimensions of the MNP ($48 \times 64 \times 48$ nm^3) remain fixed in the simulations. The microstructure is defined as a magnetite core with dimensions of $(48 - 2\delta) \times (64 - 2\delta) \times (48 - 2\delta)$ nm^3, and a maghemite shell of variable thickness δ ($\delta = 0$–10 nm); for instance, a cuboid with $\delta = 5$ nm consists of a $38 \times 54 \times 38$ nm^3 magnetite core surrounded by a 5 nm thick maghemite shell. In all cases, the $p(r)$ in Fig. 3(B) exhibit a slightly asymmetric profile, which is characterized by a linear-type rise at short distances and an extended smoother tail at larger r values, in qualitative agreement with the result for a uniformly magnetized cuboid along its easy axis. This behavior underscores the dominant uniaxial anisotropy of the cuboid as the magnetization reorients from the field direction $\vec{e}_z$ at saturation to the anisotropy axis $\vec{e}_y$ at remanence. As δ increases, the maximum of $p(r)$ decreases and shifts to smaller r values (as indicated by an arrow). The maximum of $p(r)$ shifts from $r_{max} \cong 39$ nm for the uniformly magnetized case to $r_{max} \cong 37$ nm for $\delta = 2$ nm and to the final value of $r_{max} \cong 34$ nm for $\delta = 10$ nm, indicating a reduction in the characteristic internal magnetic distances.[97,98] This observation is compatible with an increasing degree of magnetic disorder (when δ increases), as the surface layer is composed of cells with random anisotropy directions.
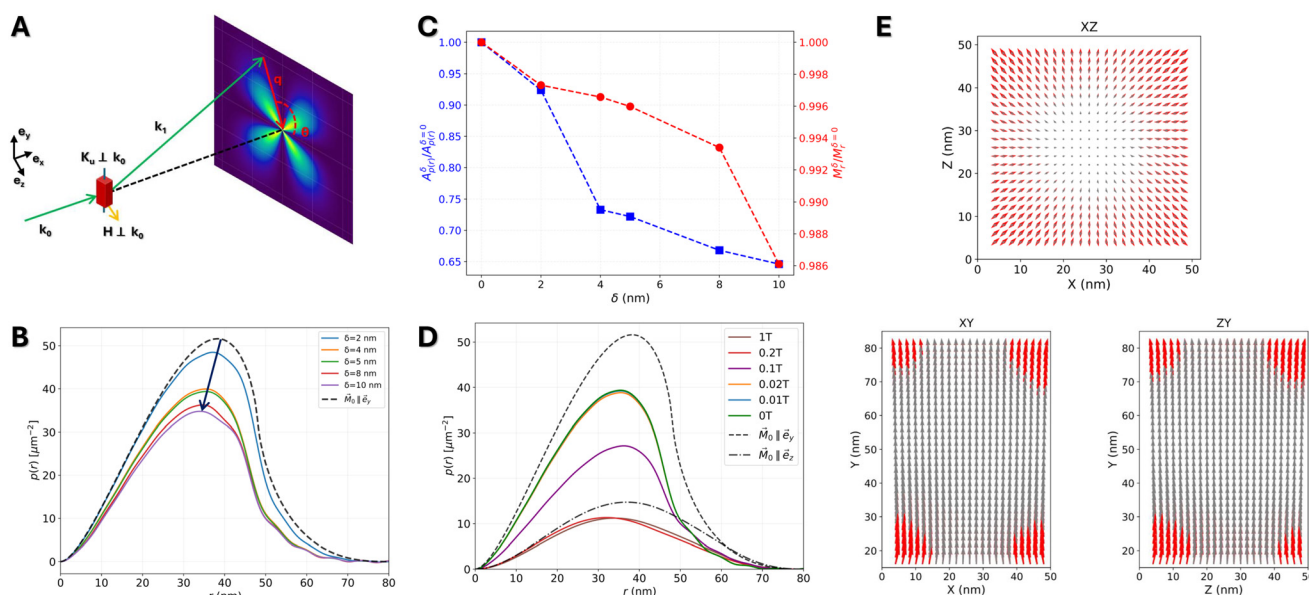
Fig. 3 (A) Schematic representation of the scattering geometry: the uniaxial anisotropy axis of the particle $\vec{K}_u$ is along the long axis of the cuboid, which is parallel (and antiparallel) to the $\vec{e}_y$ direction of a Cartesian laboratory coordinate system, and perpendicular to the wave vector $\vec{k}_0$ of the incident neutron beam ($\vec{k}_0 \parallel \vec{e}_x$). The externally applied magnetic field $\vec{H} \parallel \vec{e}_z$ is perpendicular to $\vec{K}_u$. The particle has geometric dimensions of 48 × 64 × 48 nm³ and is oriented as shown. The momentum-transfer vector $\vec{q}$ is given by $\vec{q} = \vec{k}_0 - \vec{k}_1$. (B) Pair-distance distribution functions $p(r)$ at remanence for different shell thicknesses δ (see legend). The dashed line corresponds to the extreme case where the magnetization is completely saturated along $\vec{K}_u \parallel \vec{e}_y$, calculated using eqn (6) in the SI.[43] The arrow marks the displacement of the maximum towards smaller r as δ increases. (C) Evolution of the ratio $A_{p(r)}^{\delta}/A_{p(r)}^{\delta=0}$ (left axis) and of the normalized remanent magnetization $M_r^{\delta}/M_r^{\delta=0}$ (right axis) with the interface thickness δ. (D) $p(r)$ for a series of applied fields (see legend) and for a fixed value of $\delta = 5$ nm. The black lines represent the corresponding $p(r)$ of a cuboid uniformly magnetized along $\vec{e}_z$ (dotted-dashed line) and $\vec{e}_y$ (dashed line). These were, respectively, obtained using eqn (5) and (6) in the SI.[43] (E) Remanent magnetization distributions shown for the three central planes of the cuboid ($\delta = 5$ nm). The gray arrows represent magnetic moments that are oriented along the net particle magnetization, which is mainly along $\vec{e}_y$ with small components (below 2%) along $\vec{e}_x$ and $\vec{e}_z$. The red arrows represent misaligned (canted) moments.

We propose to use the area under the $p(r)$ curve to extract quantitative information on the degree of magnetic disorder as a function of δ. It is well known from the theory of magnetic SANS that the value of the azimuthally-averaged spin–flip scattering intensity at the origin of reciprocal space, $I_{sf}(q = 0)$, and the integral of the corresponding pair-distance distribution function are related via[96]

$$I_{sf}(q = 0) = \int_0^{\infty} p(r)\mathrm{d}r = A_{p(r)}. \tag{1}$$

By taking the value at $\delta = 0$ nm as a reference, we can consider the following ratio

$$\frac{I_{sf}^{\delta}(q = 0)}{I_{sf}^{\delta=0}(q = 0)} = \frac{A_{p(r)}^{\delta}}{A_{p(r)}^{\delta=0}}, \tag{2}$$

which is compared to the normalized remanent magnetization $M_r^{\delta}/M_r^{\delta=0}$ obtained from the micromagnetic simulations. At this point, we would like to recall a crucial difference between magnetization and SANS data: while the magnetization in a conventional magnetometry experiment measures the spatially-averaged net magnetic moment of the entire particle ensemble, SANS provides Fourier-space-resolved mesoscale information of spatial correlations of the local magnetization.

As such, both techniques are complementary but not directly equivalent. Fig. 3(C) compares the evolution of the above-defined quantities as a function of δ. As expected, both decrease with increasing δ, but their trends differ markedly. Whereas the magnetization data change very weakly, by only $\cong 1.5\%$ for the largest $\delta = 10$ nm, the neutron results vary more strongly, by more than 30% for the same δ variation. These findings underscore the superior sensitivity of the SANS technique to nanoscale magnetic spin disorder. Motivated by this, and given that the quantity $I_{sf}^{\delta}(q = 0)$ is related to the average magnetization (as it is accessible in a magnetometer), future studies should aim to *quantitatively* relate the ratio eqn (2) to δ.

Fig. 3(D) displays the field dependence of $p(r)$ for an interface thickness of $\delta = 5$ nm, together with the reference curves corresponding to the uniformly magnetized cuboid along $\vec{e}_z$ and $\vec{e}_y$ (calculated from eqn (5) and (6) in the SI[43]). At the highest field ($\mu_0 H = 1$ T), the magnetization is (nearly) uniformly aligned along the $\vec{e}_z$ direction (a short axis of the cuboid), giving rise to a nearly symmetric bell-shaped $p(r)$ distribution that very closely resembles the $p(r)$ of the uniformly magnetized cuboid along $\vec{e}_z$ (black dotted-dashed line). The maximum of the $p(r)$ for $\delta = 5$ nm is slightly shifted to smaller r and slightly below the one of the uniformly magnetized

cuboid, indicating the existence of minor spin misalignment event at 1 T, which is not detectable in the magnetization measurements (compare to Fig. 2(B)). As the external field is reduced, the magnetization direction reorients from $\vec{e}_z$ towards the magnetic easy axis $\vec{K}_u \parallel \vec{e}_y$, which coincides with the long axis of the cuboid. This rotation results in a progressive asymmetry of $p(r)$ and in an increase of its overall magnitude, while the position of the maximum shifts slightly to larger r values ($r_{max}^{1T} \cong 34.0$ nm and $r_{max}^{0T} \cong 35.5$ nm) as the magnetization reorients from $\vec{e}_z$ to $\vec{e}_y$ with decreasing field. Both effects signal the development of a magnetically disordered shell at low fields, which results in a significant reduction of the characteristic magnetic distances.[97,98]

To further visualize our results, we show in Fig. 3(E) planar cuts through the 3D remanent magnetization distribution for a fixed value of $\delta = 5$ nm. The average magnetization of the cuboid is depicted by gray arrows, while the red arrows represent spins that deviate by more than 2% from the mean direction. As is seen, the magnetic disorder is primarily localized at the particle edges, where the stray field is large and induces strong torques on the magnetic moments. The spin deviations remain modest, typically less than 5%. In other words, the magnetization distribution $\vec{M}(\vec{r})$ within the core part of the cuboid is relatively uniform and the largest gradients in $\vec{M}(\vec{r})$ appear at the interface region, which represents a perturbation in the magnetic microstructure (different magnetic materials parameters and a random distribution of anisotropy axes). The spin orientation varies smoothly across the interface region and $\vec{M}(\vec{r})$ within the shell region is not randomly oriented, as the assumed anisotropy distribution might impose, but it smoothly deviates from the core direction (by less than 5%). These results suggest that polarized SANS, unlike bulk magnetometry, provides direct access to internal microstructural features that govern the magnetic behavior at the nanoscale, features that remain effectively invisible to macroscopic magnetization measurements.

4. Summary and conclusion

In this work, we have provided a micromagnetic description for the oxidation-driven transformation of magnetite to maghemite in magnetite nanoparticles. This approach captures the interplay between magnetic order and disorder at the interface and resolves the magnetization of the nanoparticles with a nanometer resolution, going beyond the conventional single-domain picture.

Our simulations incorporate dipolar interactions to capture realistic interparticle interaction effects and are benchmarked against experimental data from the magnetosome chains grown by magnetotactic bacteria. By keeping the magnetosomes within the bacteria body, the magnetic properties are preserved over an unprecedented time scale of several years. This has been cross-checked by following the oxidation process for two different bacterium strains.

Our experimental results in magnetotactic bacteria show a remarkable slower oxidation compared to the one in magnetite

nanoparticles reported in the literature (years vs. days). This fact, together with our micromagnetic results, which indicate a slower decrease of coercivity with δ at chain configurations, allows us to conclude on the beneficial role of dipolar interactions, and the related shape anisotropy, to keep the hysteresis loop broad compared to the isolated MNP situation. As a consequence, equally oxidized MNP will preserve their magnetic properties longer when they are arranged in chains, compared to their individual-particle response. We therefore propose a strategy to preserve the magnetic properties of magnetite at longer time scales by encapsulating them and letting them interact, mimicking the natural protection of the bacterial body. A very recent example for such a strategy includes the biomineralization of iron oxide in encapsulin nanocompartments by Efremova et al.[99]

Furthermore, for the example of a single oriented cuboid, we have resolved the spin distribution at the interface between magnetite and maghemite phases by numerically calculating the pair-distance distribution function $p(r)$ extracted from the polarized small-angle neutron scattering (SANS) cross section. We have connected the increase of the magnetic disorder in the shell region to the reduction of the remanent magnetization via the area under the $p(r)$ curve. Our results are compatible with a smoothly varying magnetization distribution across the shell (magnetically diffuse interface), which contrasts with the geometrically sharp interface.

The disparity between geometric and magnetic dimensions might account for the prolonged retention of magnetic functionality in partially oxidized magnetite MNPs. Our results challenge the assumption that structural oxidation boundaries directly dictate magnetic degradation, and they highlight the power of integrating micromagnetic simulations with polarized SANS to reveal hidden aspects of magnetic (dis)order in complex nanoscaled systems. Beyond its relevance for fundamental studies of disorder, this approach opens the door to characterizing magnetic nanoparticles embedded in cellular environments (which are compatible with SANS), where their performance differs significantly from that observed in extracellular experiments.[29-31]

Author contributions

Conceptualization: E. M. J. Methodology: E. M. J. Software: E. M. J., M. A., J. L. Validation: E. M. J., M. A., A. M., J. L. Formal analysis: E. M. J. Investigation: E. M. J., J. A. Sample preparation: L. G., L. M. Resources: E. M. J., J. A., A. M., J. L. Data curation: E. M. J., J. A. Visualization: E. M. J. Supervision: A. M., J. L. Project administration: E. M. J., A. M. Funding acquisition: E. M. J., A. M. Writing original draft: E. M. J. Writing, review, and editing: all authors.

Conflicts of interest

There are no conflicts to declare.

Data availability

All data supporting the findings of this study have been included within the article and as part of the supplementary information (SI). Supplementary Information contains results of the structural (TEM, XRD) and magnetic characterization of the magnetic nanoparticle samples, along with further qualitative indication for the magnetic order penetrating the shell, extracted from micromagnetic simulations. Finally, the expressions for the spin-flip SANS cross section and pair-distance distribution function are displayed. See DOI: https://doi.org/10.1039/d5nr02700d.

Acknowledgements

References

1 K. Wu, D. Su, J. Liu, R. Saha and J.-P. Wang, *Nanotechnology*, 2019, **30**, 502003.

2 H. Etemadi and P. G. Plieger, *Adv. Ther.*, 2020, **3**, 2000061.

3 A. Farzin, S. A. Etesami, J. Quint, A. Memic and A. Tamayol, *Adv. Healthcare Mater.*, 2020, **9**, 1901058.

4 R. Lapusan, R. Borlan and M. Focsan, *Nanoscale Adv.*, 2024, 2234–2259.

5 B. Rezaei, Z. Tay, S. Mostufa, O. N. Manzari, E. Azizi, S. Ciannella, H.-E.-J. Moni, C. Li, M. Zeng, J. Gomez-Pastora, *et al.*, *Nanoscale*, 2024, 11802–11824.

6 Q. A. Pankhurst, J. Connolly, S. K. Jones and J. Dobson, *J. Phys. D: Appl. Phys.*, 2003, **36**, R167.

7 Q. Pankhurst, N. Thanh, S. Jones and J. Dobson, *J. Phys. D: Appl. Phys.*, 2009, **42**, 224001.

8 B. E. Smith, P. B. Roder, X. Zhou and P. J. Pauzauskie, *Nanoscale*, 2015, **7**, 7115–7126.

9 E. A. Perigo, G. Hemery, O. Sandre, D. Ortega, E. Garaio, F. Plazaola and F. J. Teran, *Appl. Phys. Rev.*, 2015, **2**, 4.

10 D. Ortega and Q. A. Pankhurst, *Nanoscience*, 2013, **1**, e88.

11 I. Rubia-Rodríguez, A. Santana-Otero, S. Spassov, E. Tombácz, C. Johansson, P. De La Presa, F. J. Teran, M. d. P. Morales, S. Veintemillas-Verdaguer, N. T. Thanh, *et al.*, *Materials*, 2021, **14**, 706.

12 I. Castellanos-Rubio, O. Arriortua, D. Iglesias-Rojas, A. Barón, I. Rodrigo, L. Marcano, J. S. Garitaonandia, I. Orue, M. L. Fdez-Gubieda and M. Insausti, *Chem. Mater.*, 2021, **33**, 8693–8704.

13 L. H. Singh, S. Pati, E. M. Guimarães, P. Rodrigues, A. C. Oliveira and V. Garg, *Mater. Chem. Phys.*, 2016, **178**, 182–189.

14 A. F. Rodríguez, C. Moya, M. Escoda-Torroella, A. Romero, A. Labarta and X. Batlle, *J. Mater. Chem. C*, 2018, **6**, 875–882.

15 H. Sharifi Dehsari, M. Heidari, A. Halda Ribeiro, W. Tremel, G. Jakob, D. Donadio, R. Potestio and K. Asadi, *Chem. Mater.*, 2017, **29**, 9648–9656.

16 I. Morales, R. Costo, N. Mille, J. Carrey, A. Hernando and P. de la Presa, *Nanoscale Adv.*, 2021, **3**, 5801–5812.

17 D. P. Valdés, E. Lima Jr., R. D. Zysler and E. De Biasi, *Phys. Rev. Appl.*, 2020, **14**, 014023.

18 D. Serantes, K. Simeonidis, M. Angelakeris, O. Chubykalo-Fesenko, M. Marciello, M. D. P. Morales, D. Baldomir and C. Martinez-Boubeta, *J. Phys. Chem. C*, 2014, **118**, 5927–5934.

19 D. Gandia, L. Gandarias, I. Rodrigo, J. Robles-García, R. Das, E. Garaio, J. A. García, M.-H. Phan, H. Srikanth, I. Orue, J. Alonso, A. Muela and M. Fdez-Gubieda, *Small*, 2019, **15**, 1902626.

20 E. M. Jefremovas, L. Gandarias, I. Rodrigo, L. Marcano, C. Grüttner, J. A. García, E. Garayo, I. Orue, A. García-Prieto, A. Muela, M. L. Fdez-Gubierda, J. Alonso and L. Fernández Barquín, *IEEE Access*, 2021, **9**, 99552–99561.

21 K. Poon and G. Singh, *Appl. Mater. Today*, 2025, **44**, 102787.

22 F. Mickoleit, C. Jörke, R. Richter, S. Rosenfeldt, S. Markert, I. Rehberg, A. S. Schenk, O. Bäumchen, D. Schüler and J. H. Clement, *Small*, 2023, **19**, 2206244.

23 T. Kim, S. Sim, S. Lim, M. A. Patino, J. Hong, J. Lee, T. Hyeon, Y. Shimakawa, S. Lee, J. P. Attfield, *et al.*, *Nat. Commun.*, 2021, **12**, 6356.

24 S. Schwaminger, D. Bauer, P. Fraga-García, F. Wagner and S. Berensmeier, *CrystEngComm*, 2017, **19**, 246–255.

25 J. Watt, A. R. Poerwoprajitno, Y. Gandhi, C. B. Carter, D. L. Huber and R. Kalia, *Microsc. Microanal.*, 2025, **31**, ozaf048–ozaf693.

26 Z. Nedelkoski, D. Kepaptsoglou, L. Lari, T. Wen, R. A. Booth, S. D. Oberdick, P. L. Galindo, Q. M. Ramasse, R. F. Evans, S. Majetich, *et al.*, *Sci. Rep.*, 2017, **7**, 45997.

27 E. C. Vreeland, J. Watt, G. B. Schober, B. G. Hance, M. J. Austin, A. D. Price, B. D. Fellows, T. C. Monson, N. S. Hudak, L. Maldonado-Camargo, *et al.*, *Chem. Mater.*, 2015, **27**, 6059–6066.

28 A. U. Gehring, M. Charilaou and I. García-Rubio, *J. Magn. Magn. Mater.*, 2012, **324**, 1281–1284.

29 G. M. Calaf, U. Urzua, L. Termini and F. Aguayo, *Oncotarget*, 2018, **9**, 23824.

30 I. Parolini, C. Federici, C. Raggi, L. Lugini, S. Palleschi, A. De Milito, C. Coscia, E. Iessi, M. Logozzi, A. Molinari, *et al.*, *J. Biol. Chem.*, 2009, **284**, 34211–34222.

31 L. Gandarias, A. G. Gubieda, G. Gorni, O. Mathon, L. Olivi, A. Abad Díaz de Cerio, M. L. Fdez-Gubieda, A. Muela and A. García-Prieto, *Biotechnol. J.*, 2023, **18**, 2300173.

32 D. Faivre and D. Schuler, *Chem. Rev.*, 2008, **108**, 4875–4898.

33 A. Fischer, M. Schmitz, B. Aichmayer, P. Fratzl and D. Faivre, *J. R. Soc., Interface*, 2011, **8**, 1011–1018.

34 L. Marcano, I. Orue, D. Gandia, L. Gandarias, M. Weigand, R. M. Abrudan, A. García-Prieto, A. García-Arribas, A. Muela, M. L. Fdez-Gubieda and S. Valencia, *ACS Nano*, 2022, **16**, 7398–7408.

35 M. L. Fdez-Gubieda, A. Muela, J. Alonso, A. García-Prieto, L. Olivi, R. Fernandez-Pacheco and J. M. Barandiarán, *ACS Nano*, 2013, **7**, 3297–3305.

36 D. Gandia, L. Marcano, L. Gandarias, D. Villanueva, I. Orue, R. M. Abrudan, S. Valencia, I. Rodrigo, J. A. García, A. Muela, M. L. Fdez-Gubieda and J. Alonso, *ACS Appl. Mater. Interfaces*, 2022, **15**, 566–577.

37 N. Kent, C. Gates, B. Senyuk, J. B. t. Hove, J. Cameron and I. I. Smalyukh, *Phys. Rev. E*, 2025, **112**, 044411.

38 D. Zákutná, D. Nižňanský̀, L. C. Barnsley, E. Babcock, Z. Salhi, A. Feoktystov, D. Honecker and S. Disch, *Phys. Rev. X*, 2020, **10**, 031019.

39 A. Michels, *Magnetic Small-Angle Neutron Scattering: A Probe for Mesoscale Magnetism Analysis*, Oxford University Press, Oxford, 2021.

40 D. Honecker, M. Bersweiler, S. Erokhin, D. Berkov, K. Chesnel, D. A. Venero, A. Qdemat, S. Disch, J. K. Jochum, A. Michels, *et al.*, *Nanoscale Adv.*, 2022, **4**, 1026–1059.

41 A. Lak, S. Disch and P. Bender, *Adv. Sci.*, 2021, **8**, 2002682.

42 M. Gerina, M. Sanna Angotzi, V. Mameli, M. Mazur, N. Rusta, E. Balica, P. Hrubovcak, C. Cannas, D. Honecker and D. Zákutná, *ACS Appl. Nano Mater.*, 2024, **7**, 27210–27216.

43 The SI provides further details on the structural and magnetic characterization of the magnetite MNPs and displays the main expressions for the spin–flip SANS cross section and pair-distance distribution function.

44 U. Heyen and D. Schüler, *Appl. Microbiol. Biotechnol.*, 2003, **61**, 536–544.

45 A. Vansteenkiste, J. Leliaert, M. Dvornik, M. Helsen, F. Garcia-Sanchez and B. Van Waeyenberge, *AIP Adv.*, 2014, **4**, 10.

46 D. Gandia, L. Marcano, L. Gandarias, A. G. Gubieda, A. García-Prieto, L. Fernández Barquín, J. I. Espeso, E. M. Jefremovas, I. Orue, A. Abad Diaz de Cerio, M. L. Fdez-Gubieda and J. Alonso, *ACS Omega*, 2025, **10**, 16061.

47 A. Witt, K. Fabian and U. Bleil, *Earth Planet. Sci. Lett.*, 2005, **233**, 311–324.

48 E. Jefremovas, L. Gandarias, L. Marcano, A. Gacía-Prieto, I. Orue, A. Muela, M. Fdez-Gubieda, L. F. Barquín and J. Alonso, *Nanoscale Adv.*, 2022, **4**, 2649–2659.

49 I. Orue, L. Marcano, P. Bender, A. García-Prieto, S. Valencia, M. Mawass, D. Gil-Cartón, D. A. Venero, D. Honecker, A. García-Arribas, *et al.*, *Nanoscale*, 2018, **10**, 7407–7419.

50 J. Leliaert, B. Van de Wiele, A. Vansteenkiste, L. Laurson, G. Durin, L. Dupré and B. Van Waeyenberge, *J. Appl. Phys.*, 2014, **115**, 233903.

51 K. P. Lam, A. P. Hitchcock, M. Obst, J. R. Lawrence, G. D. Swerhone, G. G. Leppard, T. Tyliszczak, C. Karunakaran, J. Wang, K. Kaznatcheev, *et al.*, *Chem. Geol.*, 2010, **270**, 110–116.

52 M. Widdrat, M. Kumari, É. Tompa, M. Pósfai, A. M. Hirt and D. Faivre, *ChemPlusChem*, 2014, **79**, 1225–1233.

53 A. Rečnik, I. Nyírő-Kósa, I. Dódony and M. Pósfai, *CrystEngComm*, 2013, **15**, 7539–7547.

54 L. Exl, S. Bance, F. Reichel, T. Schrefl, H. P. Stimming and N. J. Mauser, *J. Appl. Phys.*, 2014, **115**, 17D118.

55 L. G. Vivas, R. Yanes, D. Berkov, S. Erokhin, M. Bersweiler, D. Honecker, P. Bender and A. Michels, *Phys. Rev. Lett.*, 2020, **125**, 117201.

56 E. Pratami Sinaga, M. P. Adams, M. Bersweiler, L. G. Vivas, E. H. Hasdeo, J. Leliaert, P. Bender, D. Honecker and A. Michels, *Phys. Rev. B*, 2023, **107**, 014416.

57 M. P. Adams, E. P. Sinaga, Š. Liščák and A. Michels, *Phys. Rev. B*, 2024, **110**, 014420.

58 E. P. Sinaga, M. P. Adams, E. H. Hasdeo and A. Michels, *Phys. Rev. B*, 2024, **110**, 054404.

59 D. Honecker, A. Ferdinand, F. Döbrich, C. D. Dewhurst, A. Wiedenmann, C. Gómez-Polo, K. Suzuki and A. Michels, *Eur. Phys. J. B*, 2010, **76**, 209–213.

60 K. L. Krycka, J. A. Borchers, R. A. Booth, Y. Ijiri, K. Hasz, J. J. Rhyne and S. A. Majetich, *Phys. Rev. Lett.*, 2014, **113**, 147203.

61 D. Zákutná, D. Nižňanský, L. C. Barnsley, E. Babcock, Z. Salhi, A. Feoktystov, D. Honecker and S. Disch, *Phys. Rev. X*, 2020, **10**, 031019.

62 A. Malyeyev, I. Titov, C. Dewhurst, K. Suzuki, D. Honecker and A. Michels, *J. Appl. Crystallogr.*, 2022, **55**, 569–585.

63 V. Ukleev, F. Ajejas, A. Devishvili, A. Vorobiev, N.-J. Steinke, R. Cubitt, C. Luo, R.-M. Abrudan, F. Radu, V. Cros, N. Reyren and J. S. White, *STAM Methods*, 2024, **25**, 2315015.

64 F. Walz, *J. Phys.: Condens. Matter*, 2002, **14**, R285.

65 Q. Yu, A. Mottaghizadeh, H. Wang, C. Ulysse, A. Zimmers, V. Rebuttini, N. Pinna and H. Aubin, *Phys. Rev. B: Condens. Matter Mater. Phys.*, 2014, **90**, 075122.

66 L. Marcano, A. García-Prieto, D. Muñoz, L. F. Barquín, I. Orue, J. Alonso, A. Muela and M. Fdez-Gubieda, *Biochim. Biophys. Acta, Gen. Subj.*, 2017, **1861**, 1507–1514.

67 D. Gandia, L. Gandarias, L. Marcano, I. Orue, D. Gil-Cartón, J. Alonso, A. García-Arribas, A. Muela and M. L. Fdez-Gubieda, *Nanoscale*, 2020, **12**, 16081–16090.

68 S. Laurent, J.-L. Bridot, L. Vander Elst and R. N. Muller, *Future Med. Chem.*, 2010, **2**, 427–449.

69 *Iron Oxides: From Nature to Applications*, ed. D. Faivre, John Wiley and Sons, Ltd, 2016.

70 A. Millan, A. Urtizberea, N. Silva, F. Palacio, V. Amaral, E. Snoeck and V. Serin, *J. Magn. Magn. Mater.*, 2007, **312**, L5–L9.

71 A. Muela, D. Munoz, R. Martín-Rodríguez, I. Orue, E. Garaio, A. Abad Diaz de Cerio, J. Alonso, J. A. García and M. L. Fdez-Gubieda, *J. Phys. Chem. C*, 2016, **120**, 24437–24448.

72 D. Muñoz, L. Marcano, R. Martín-Rodríguez, L. Simonelli, A. Serrano, A. García-Prieto, M. Fdez-Gubieda and A. Muela, *Sci. Rep.*, 2020, **10**, 11430.

73 J. Wan, R. Ji, J. Liu, K. Ma, Y. Pan and W. Lin, *Cell Rep.*, 2024, **43**, 12.

74 M. Amor, F. P. Mathon, C. L. Monteil, V. Busigny and C. T. Lefevre, *Environ. Microbiol.*, 2020, **22**, 3611–3632.

75 H. Nudelman, Y.-Z. Lee, Y.-L. Hung, S. Kolusheva, A. Upcher, Y.-C. Chen, J.-Y. Chen, S.-C. Sue and R. Zarivach, *Front. Microbiol.*, 2018, **9**, 2480.

76 S. Ben-Shimon, D. Stein and R. Zarivach, *J. Struct. Biol.: X*, 2021, **5**, 100052.

77 M. Fdez-Gubieda, J. Alonso, A. García-Prieto, A. García-Arribas, L. Fernández Barquín and A. Muela, *J. Appl. Phys.*, 2020, **128**, 070902.

78 M. L. Fdez-Gubieda, L. Marcano, A. Muela, A. García-Prieto, J. Alonso and I. Orue, in *Nature Driven Magnetic Nanoarchitectures*, ed. D. Peddis, S. Laureti and D. Fiorani, Springer International Publishing, Cham, 2021, pp. 159–179.

79 M. Amor, V. Busigny, P. Louvat, M. Tharaud, A. Gélabert, P. Cartigny, J. Carlut, A. Isambert, M. Durand-Dubief, G. Ona-Nguema, *et al.*, *Geochim. Cosmochim. Acta*, 2018, **232**, 225–243.

80 A. G. Roca, J. F. Marco, M. d. P. Morales and C. J. Serna, *J. Phys. Chem. C*, 2007, **111**, 18577–18584.

81 D. Fiorani, A. Testa, F. Lucari, F. D'orazio and H. Romero, *Phys. B*, 2002, **320**, 122–126.

82 D. A. Bazylinski, R. B. Frankel and H. W. Jannasch, *Nature*, 1988, **334**, 518.

83 K. T. Silva, P. E. Leão, F. Abreu, J. A. López, M. L. Gutarra, M. Farina, D. A. Bazylinski, D. M. Freire and U. Lins, *Appl. Environ. Microbiol.*, 2013, **79**, 2823–2827.

84 S. S. Kalirai, D. A. Bazylinski and A. P. Hitchcock, *PLoS One*, 2013, **8**, e53368.

85 C. Tannous and J. Gieraltowski, *Eur. J. Phys.*, 2008, **29**, 475.

86 M. F. de Campos, F. A. Sampaio da Silva, E. A. Perigo and J. A. de Castro, *J. Magn. Magn. Mater.*, 2013, **345**, 147–152.

87 D. Channing and M. Graham, *Corros. Sci.*, 1972, **12**, 271–289.

88 C. A. Gorski and M. M. Scherer, *Am. Mineral.*, 2010, **95**, 1017–1026.

89 T. P. Almeida, A. R. Muxworthy, T. Kasama, W. Williams, C. Damsgaard, C. Frandsen, T. J. Pennycook and R. E. Dunin-Borkowski, *Geochem., Geophys., Geosyst.*, 2015, **16**, 2969–2979.

90 I. Bonková, M. Miglierini, M. Bujdoš and M. Kopáni, *Acta Phys. Pol. A*, 2017, **131**, 1081–1083.

91 S. Mühlbauer, D. Honecker, É. A. Périgo, F. Bergner, S. Disch, A. Heinemann, S. Erokhin, D. Berkov, C. Leighton, M. R. Eskildsen, *et al.*, *Rev. Mod. Phys.*, 2019, **91**, 015004.

92 S. Disch, E. Wetterskog, R. P. Hermann, A. Wiedenmann, U. Vainio, G. Salazar-Alvarez, L. Bergström and T. Brückel, *New J. Phys.*, 2012, **14**, 013025.

93 K. L. Krycka, R. A. Booth, C. R. Hogg, Y. Ijiri, J. A. Borchers, W. Chen, S. Watson, M. Laver, T. R. Gentile, L. R. Dedon, *et al.*, *Phys. Rev. Lett.*, 2010, **104**, 207203.

94 K. L. Krycka, J. A. Borchers, R. Booth, Y. Ijiri, K. Hasz, J. J. Rhyne and S. Majetich, *Phys. Rev. Lett.*, 2014, **113**, 147203.

95 P. Bender, L. Marcano, I. Orue, D. A. Venero, D. Honecker, L. F. Barquín, A. Muela and M. L. Fdez-Gubieda, *Nanoscale Adv.*, 2020, **2**, 1115–1121.

96 D. I. Svergun and M. H. J. Koch, *Rep. Prog. Phys.*, 2003, **66**, 1735.

97 M. P. Adams, A. Michels and H. Kachkachi, *Appl. Crystallogr.*, 2022, **55**, 1488–1499.

98 M. P. Adams, A. Michels and H. Kachkachi, *Appl. Crystallogr.*, 2022, **55**, 1475–1487.

99 M. V. Efremova, U. Wiedwald, F. Sigmund, S.-V. Bodea, H. Ohldag, T. Feggeler, R. Meckenstock, L. N. Panzl, J. Francke, I. Beer, *et al.*, *Adv. Funct. Mater.*, 2025, **35**, 2418013.